Thermal Science and Engineering 2025, 8(2), 11618.
https://doi.org/10.24294/tse11618

Article

ANN-aided optimization study on thermal performance and energy consumption of an industrial shell-and-tube heat exchanger system

Sahin Gungor

Department of Mechanical Engineering, Izmir Katip Celebi University, Izmir 35620, Turkey; sahin.gungor@ikcu.edu.tr

CITATION

Gungor S. ANN-aided optimization study on thermal performance and energy consumption of an industrial shell-and-tube heat exchanger system. Thermal Science and Engineering. 2025; 8(2): 11618. https://doi.org/10.24294/tse11618

ARTICLE INFO

Received: 21 March 2025
Accepted: 25 April 2025
Available online: 28 May 2025

Abstract: Global energy agencies and commissions report a sharp increase in energy demand based on commercial, industrial, and residential activities. At this point, we need energy-efficient and high-performance systems to maintain a sustainable environment. More than 30% of the generated electricity has been consumed by HVAC-R units, and heat exchangers are the main components affecting the overall performance. This study combines experimental measurements, numerical investigations, and ANN-aided optimization studies to determine the optimal operating conditions of an industrial shell and tube heat exchanger system. The cold/hot stream temperature level is varied between 10 ℃ and 50 ℃ during the experiments and numerical investigations. Furthermore, the flow rates are altered in a range of 50–500 L/h to investigate the thermal and hydraulic performance under laminar and turbulent regime conditions. The experimental and numerical results indicate that U-tube bundles dominantly affect the total pumping power; therefore, the energy consumption experienced at the cold side is about ten times greater the one at the hot side. Once the required data sets are gathered via the experiments and numerical investigations, ANN-aided stochastic optimization algorithms detected the C10H50 scenario as the optimal operating case when the cold and hot stream flow rates are at 100 L/h and 500 L/h, respectively.

Keywords: shell-and-tube heat exchanger; thermal performance; energy consumption; stochastic optimization; artificial neural network

1. Introduction

The United Nations Climate Change Conference (COP27) gathered countries to come up with solutions on how to eliminate the carbon footprint resulting from industrial processes, transportation, and human activities [1]. Electrification has been detected as a dominant factor in the carbon footprint, as the share of renewable energy sources in the global electricity generation is only about 28.7% [2]. At this point, heating, ventilation, air-conditioning, and refrigeration (HVAC-R) systems used in residential buildings and industrial applications are responsible for a large amount of carbon emission, as more than 30% of the generated electricity has been consumed by the building HVAC-R units [3–5].

Energy consumption of HVAC-R and any sort of heat recovery systems can be reduced via more efficient heat exchanger systems [6,7]. In HVAC-R heat exchanger systems, two or more fluids interact in liquid-liquid [8–10], liquid-gas [11,12] or gas-gas [13–15] phases to exchange heat through the heat transfer surfaces. Heat exchangers may be classified according to the geometry, fluid phase, contact type, flow arrangement, or number of fluids, and they shall be properly selected according to the application needs. Note that thermophysical properties of the selected heat exchange materials, type and volume of the operating fluids, flow rates of the cold and

hot streams, and heat transfer surface affect the thermal performance and energy consumption of the investigated heat exchanger systems [16,17]. In counterflow heat exchanger arrangements, a more uniform temperature difference exists throughout the heat transfer path; therefore, these systems are always more efficient than the parallel flow [18–20]. Cross-flow systems are an alternative to counter-flow, and this arrangement is commonly preferred in heat recovery ventilation applications, fan coils, and shell-and-tube heat exchangers [21,22].

Shell and tube heat exchangers are dominantly preferred in power plants, energy, and petrochemical industries due to their superior robustness and large heat transfer surface area [23]. Furthermore, these systems allow operating at high pressures while exchanging heat in an efficient way. Ozden and Tari [24] numerically investigated the effects of shell diameter, baffle spacing, and baffle cut on shell-side thermal performance. They compared the thermal outputs of Spalart–Allmaras, standard k-ε, and realizable k-ε turbulence models, and the results indicated that realizable k-ε fit best to the analytical results obtained via the logarithmic mean temperature difference method. Wang et al. [25] focused on a multiple shell-pass shell-and-tube heat exchanger combined with continuous helical baffles. The numerical findings showed that the pressure drop of the proposed combined system is about 13% lower than the segmental baffled shell and tube heat exchanger. Likewise, various shell and tube baffle designs were compared by Arani and Moradi from thermal performance and pressure loss points of view [26]. The numerical results indicate that the disk baffle shell and tube heat exchanger with longitudinal triangular ribbed tube has higher performance among the other combinations. On the other hand, Gao et al. [27] experimentally examined the thermal and hydraulic performance of shell-and-tube heat exchangers with discontinuous helical baffles. The baffle helix angle was varied between 8° and 40°, and it is concluded that the total pressure drop decreases with helix angle increment. Furthermore, the highest thermal performance was observed at a 40° baffle helix angle. Furthermore, many researchers performed optimization studies on shell and tube heat exchanger systems to obtain optimal design or best operating point under determined system constraints [28–30].

This study mainly focuses on the thermal performance and energy consumption of an industrial shell and tube heat exchanger system. In spite of the fact that numerous numerical studies have been performed by researchers, the combination of the experimental measurements, numerical investigations, and ANN-aided stochastic optimization is a novel technique to obtain optimal operating conditions for shell and tube heat exchanger systems. First, experimental investigations have been conducted under laminar and turbulent regime conditions to determine the heat transfer rate and pressure drop experienced within the shell side and U-tube bundles. Next, the proposed numerical model is validated via the collected experimental data just after a comprehensive mesh independency study. Nonlinear stochastic optimization algorithms of Differential Evolution (DE), Nelder-Mead (NM), Random Search (RS), and Simulated Annealing (SA) are utilized during the ANN-aided optimization processes to obtain the best operating point satisfying enhanced thermal performance and lower energy consumption.

2. Method and models

2.1. Experimental investigations

Experiments of an industrial shell and tube heat exchanger were conducted within a thermally controlled laboratory maintained at 20 ℃. The temperature uncertainty of the thermostatic control system is about ±0.4 ℃. **Figure 1** shows the geometrical details and conceptual projection of the investigated heat exchanger system. Hot fluid enters the shell from an 18 mm diameter inlet, and the distance between the identical shell inlet and outlet centerlines is 140 mm. The shell diameter is 114.3 mm (45″), and it contains four segmental baffles to provide enhanced heat transfer between the tubes and shell sides.

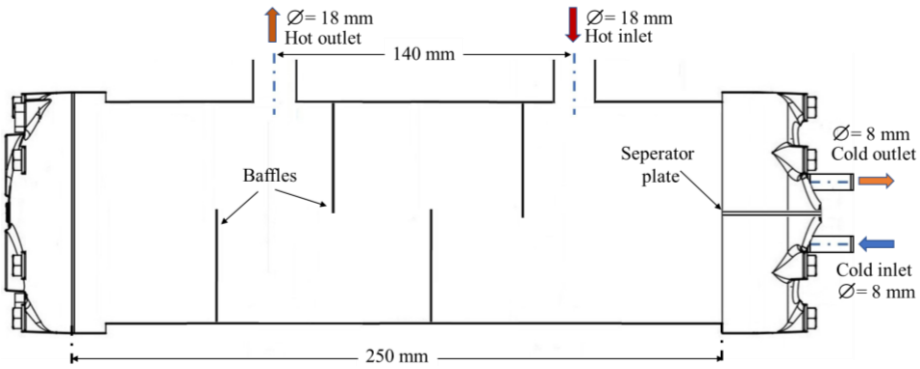

Figure 1. Geometrical details of the investigated shell and tube heat exchanger.

The tube side has 16 U-turn tubes having an identical diameter of 9.52 mm (3/8″). The tube inlets are located on the bottom half of the right cap, while the outlets are on the top to ensure cross-counter flow (**Figure 1**). Note that the diameters of the cold stream inlet and outlet are 8 mm, and a stainless-steel separator plate provides sealing between these sections. **Table 1** presents the main technical specifications of the investigated shell and tube heat exchanger system. Copper tubes are preferred for providing higher heat transfer performance, while stainless steel shells have been chosen for robustness.

Table 1. Technical specifications of the investigated shell and tube heat exchanger.

Section	Material type	Limit pressure	Temperature range	Diameter	Length	Number of tubes/baffles
Tubes	Copper	12 bar	−10/+90 ℃	3/8″	250 mm	16 U-type
Shell side	Stainless steel	25 bar	−10/+90 ℃	45″	310 mm	4 segmental

Experimental investigations for observing the thermal and hydraulic performance of the shell and tube heat exchanger system are conducted at various temperature levels and mass flow rates. The experimental setup configuration and main electrical/thermal components used during the experiments are presented in **Figure 2**. As documented in the previous study [31], cold stream temperature level is precisely controlled via a refrigerated-heating circulator (Labo, C400-H23 model). Thermal capacities of the circulator are 0.4 kW in cooling and 2 kW in heating operations, respectively. Note that the cold stream outlet fed the hydraulic bench (TQ Instruments, H1D model) to maintain the circulator temperature level at a certain operating point.

On the other hand, hot water is supplied by an additional closed loop having two 2.5 kW electric heaters. The closed hot water system contains a centrifugal pump (Halm, U130 model) having a three-level flow switch and an expansion tank (Cruwa, CRW 2S model).

Figure 2. Experimental setup configuration and main components/devices.

Temperature levels of the cold and hot streams are collected via PT100 probes and data loggers (IMC, Cs-7008 model, and Delta Electronics, DOP-AS35THTD model). The probes are calibrated with the help of a precise thermal bath to avoid measurement discrepancies and errors. The measured temperature levels are monitored on the digital display to check whether the operations reach a steady-state regime. Once the temperature variations are less than 1%, the outlet temperatures of the cold and hot streams are reported. Note that the pipelines are made of thermally low conductive thermoplastics to eliminate the thermal losses as much as possible. Furthermore, the inlet-outlet lines of the shell and tube heat exchanger system are wrapped with polyurethane foam for thermal insulation. The cold stream temperature at the inlet varies between 10 ℃ and 30 ℃, while the hot water inlet has been changed in a range of 20 ℃ to 50 ℃.

Mass flow rate is another critical parameter affecting the thermal performance and pumping power of the investigated heat exchanger system. In this study, the volumetric flow rate of the cold and hot water streams varies between 50 L/h and 500 L/h to observe the heat transfer rates and pressure drop under laminar and turbulent

regime conditions. Pressure levels at the inlet and outlet of the cold and hot water lines are measured by the manometers (Pakkens, SH 0532 model). Furthermore, a digital multimeter system (EPM-06, RMS model) measuring the phase angle (cos ϕ) and minimum-maximum values is utilized to report the power consumption of the heaters and pump.

2.2. Uncertainty analysis

In the experimental investigations, determination of the uncertainties within the experimental setup is crucial, as the measurement devices and components have an accuracy margin [31,32]. In this study, an uncertainty analysis was performed to determine the percentage of measurement error margin for each experimental component. The user manuals and manufacturer guides are examined in detail to obtain the accuracy range of the measurement systems. In addition, the measurement performance of the PT100 probes, one of the most critical components in the experiments, is determined via a precise thermal bath to eliminate possible discrepancies in the temperature data. **Table 2** shows the critical specifications and uncertainty ranges of the measurement systems used in the experimental investigations. The findings indicate that both the data logger and the refrigerated circulator systems have a measurement accuracy with less than a 0.5% error margin. The uncertainty percentage of the manometers, PT100 temperature probes, and digital multimeter is in a range of 1%–2%.

Table 2. Uncertainty analysis of the experimental measurements.

Equipment	Specifications	Uncertainty
Refrigerated circulator	−40 ℃ to 100 ℃ temperature range 0.4 kW cooling, 2 kW heating capacity 8 L fluid reservoir PID controller and digital display	± 0.03 ℃
PT100 probes	−50 ℃ to 300 ℃ temperature range 100 Ω resistance at 0 ℃	± 1.75%
Multimeter	2–120 A current measurement 10–300 V voltage range Phase angle (cos ϕ) monitoring	1% ± 1 digit
Datalogger	8 measurement channels in parallel Up to 100 kHz sampling rate IMC Studio software for data-processing	± 0.4%
Manometers	120 ℃ maximum fluid temperature 4 bar maximum pressure Complies with EN 837-3 standard	± 1.6%

In addition to the individual error margins, the joint uncertainty levels are determined for the integrated measurement systems, such as PT100 temperature probes and data logger. The maximum level is calculated as less than 2.34% for each investigated flow/thermal scenario. Furthermore, inequality between the cold and hot

stream heat transfer rates is considered, and it is calculated as less than 1.27%. Note that the experiments have been re-conducted three times under the identical boundary and initial conditions to avoid possible measurement errors.

2.3. Validation and numerical investigations

Once the experiments are completed for all thermal and hydraulic scenarios, an identical numerical model of the investigated shell and tube heat exchanger system is created. The numerical model has the same dimensions as the examined heat exchanger system, and initial/boundary conditions are defined in conformity with the experiments to ensure the identical physical phenomena.

The outer surfaces of the numerical model are set under natural convection conditions with an ambient temperature of 20 ℃ as the laboratory temperature was kept at this level during the experiments. U-turn tubes, four segmental baffles, and separator sections are placed in the shell in appropriate positions. Likewise, inlet/outlet regions of the cold and hot water streams are modeled according to the geometrical details of the investigated shell and tube heat exchanger system. The volumetric flow rate is varied in a range of 50–500 L/h to examine the thermal and hydraulic performance under both laminar and turbulent flow regime conditions. The cold stream inlet temperature has varied between 10 ℃ and 30 ℃, while the hot water inlet has been altered in a range of 20 ℃ to 50 ℃. ANSYS Fluent software is utilized for the modelling and simulations. **Figure 3** presents the computational domain and main components of the investigated numerical model.

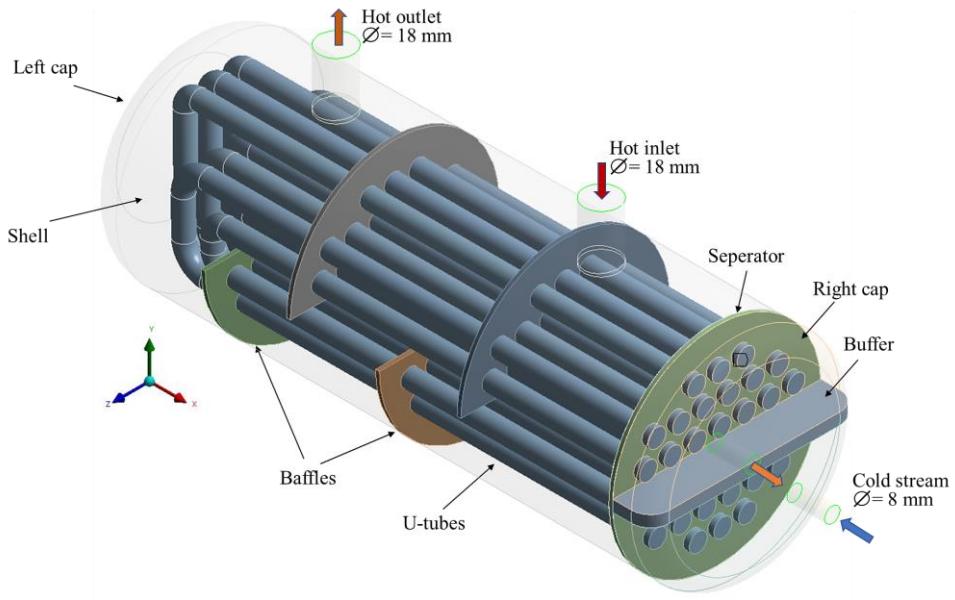

Figure 3. Three-dimensional computational domain.

Here, the energy equation was coupled with fluid flow physics under both laminar and turbulent flow regimes. The temperature field in the shell and tube heat exchanger system and the coolant velocity fields were determined by solving the conservation equations of mass, momentum, and energy in a steady-state regime. Under laminar flow conditions, the governing equation set is given as follows [33,34]:

$$\nabla . V = \frac{\partial u}{\partial x} + \frac{\partial v}{\partial y} + \frac{\partial w}{\partial z} = 0 \quad (1)$$

$$\rho_f \frac{DV}{Dt} = -\nabla P + \mu_f \nabla^2 V + g \quad (2)$$

$$\frac{DT}{Dt} = \alpha \nabla^2 T \quad (3)$$

where ***V*** corresponds to the velocity vector, *D*/*Dt* stands for the material derivative, and the subscript *f* is for fluid. ρ is the density, *P* is the pressure, μ is the dynamic viscosity, g is the gravitational acceleration, α is the thermal diffusivity, and *T* denotes the temperature. The Reynolds-averaged Navier-Stokes (RANS) model has been utilized to move the turbulence flow regime investigations. The RANS equations given below are derived by taking a time average of the Navier-Stokes equations [34,35].

$$\nabla . \underline{V} = \frac{\partial \underline{u}}{\partial x} + \frac{\partial \underline{v}}{\partial y} + \frac{\partial \underline{w}}{\partial z} = 0 \quad (4)$$

$$\rho_f \frac{DV}{Dt} + \rho_f \frac{\partial}{\partial x_j} (\underline{u_i' u_j'}) = -\nabla P + \mu_f \nabla^2 V + \vec{g} \quad (5)$$

$$\frac{DT}{Dt} = \alpha \nabla^2 T - \frac{\partial (\underline{u'T'})}{\partial x} - \frac{\partial (\underline{v'T'})}{\partial y} - \frac{\partial (\underline{w'T'})}{\partial z} \quad (6)$$

where $\underline{u}$, $\underline{v}$, $\underline{w}$, and $\underline{T}$ are the average velocity components in each direction and mean temperature, respectively. After the validation study (**Table 3**), the *k*-ε turbulence model was chosen as the viscous turbulence model due to high consistency with the experimental results. Main equations of the *k*-ε turbulence model are as follows [35,36]:

$$\frac{\partial k}{\partial t} + u_i \frac{\partial k}{\partial x_i} = \frac{\mu_t}{\rho} S^2 - \varepsilon + \frac{\partial}{\partial x_j} \left[\frac{1}{\rho} \left(\mu + \frac{\mu_t}{\sigma_k} \right) \frac{\partial k}{\partial x_j} \right] \quad (7)$$

$$\frac{\partial \varepsilon}{\partial t} + u_i \frac{\partial \varepsilon}{\partial x_i} = \frac{\varepsilon}{k} \left(C_1 \frac{\mu_t}{\rho} S^2 - \varepsilon C_2 \right) + \frac{\partial}{\partial x_j} \left[\frac{1}{\rho} \left(\mu + \frac{\mu_t}{\sigma_\varepsilon} \right) \frac{\partial \varepsilon}{\partial x_j} \right] \quad (8)$$

$$\mu_t = \rho C_\mu \frac{k^2}{\varepsilon} \quad (9)$$

where k, ε and μ_t are the turbulence kinetic energy term, eddy dissipation rate, and eddy viscosity, respectively. σ_k and σ_ε correspond to the turbulent Prandtl numbers for k and ε. S is the source term, while the C_μ, C_1 and C_2 are the model constants, which are $C_\mu = 0.09, C_1 = 1.44, C_2 = 1.92$ [36]. Note that the initial and boundary conditions applied in the numerical model are identical to the experimental investigation. The numerical solutions are based on the SIMPLE algorithm. The mesh size was varied between 1.6×10^6 and 6.8×10^6 for the entire three-dimensional domain to achieve an independent mesh structure. The criteria chosen were outlet

temperature values of the cold and hot streams. **Figure 4** shows the mesh independency study results based on various thermal scenarios. Cold and hot streams are abbreviated by C and H, while the number indicates the temperature level in degrees Celsius. According to the cold and hot outlet temperature variations, the mesh structure having about 4.98 × 10^6 mesh elements was selected to reduce the computational burden while ensuring mesh independency.

Table 3. Validation study temperature results (°C) for various turbulence models.

	Experimental results	**Standard *k-ε***	**Realizable *k-ε***	**Standard *k-w***	**SST *k-w***	**Min. Discrepancy**
	100 L/h flow rate at the cold and hot streams					
C10-H20	14.81	14.88	14.71	14.69	14.96	0.47%
C10-H30	19.36	19.51	19.53	18.95	19.57	0.62%
C10-H40	24.08	23.93	23.87	23.84	23.84	0.79%
C10-H50	28.69	28.17	28.11	28.29	28.22	1.39%
	150 L/h flow rate at the cold and hot streams					
C10-H20	14.69	14.83	14.88	14.85	14.51	0.95%
C10-H30	19.42	19.11	19.06	19.74	19.08	1.49%
C10-H40	24.13	24.39	23.97	24.41	24.38	0.61%
C10-H50	30.12	29.24	29.08	29.04	29.11	2.92%
	200 L/h flow rate at the cold and hot streams					
C10-H20	14.94	14.78	14.77	15.85	15.12	1.12%
C10-H30	19.41	19.68	19.34	20.03	19.94	1.39%
C10-H40	24.19	24.06	24.42	23.87	24.48	0.54%
C10-H50	28.32	28.63	29.11	28.17	29.29	1.08%

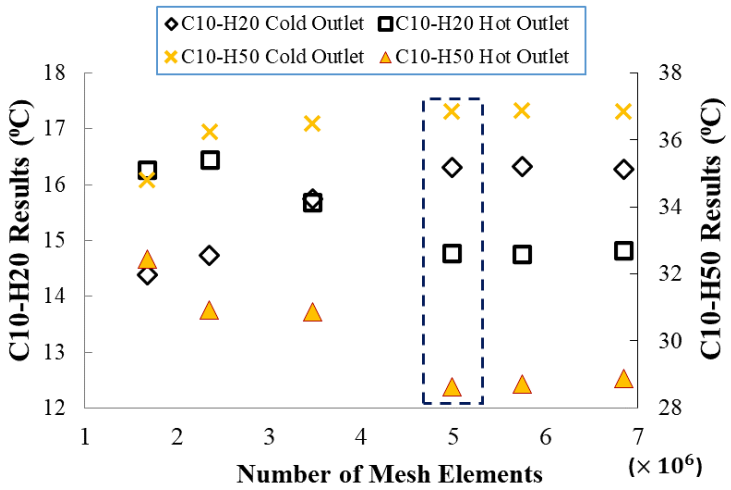

Figure 4. Mesh independency study results for cold temperature of 10 °C (C10) versus minimum (H10) and maximum (H50) hot stream temperature levels.

Validation of the proposed numerical model was examined under various turbulence model alternatives to obtain an improved consistency between the numerical and experimental results. In the validation study, cold stream temperature was determined as 10 °C (C10), while the hot water temperature level within the shell

was altered between 20 ℃ (H20) and 50 ℃ (H50), and variations on the hot stream outlet were investigated via standard *k*-*ε*, realizable *k*-*ε*, standard *k*-*w*, and SST *k*-*w* turbulence models. The change in the viscosity and specific heat capacity was also considered (**Figure 5**) to calculate accurate Reynolds numbers and heat transfer rates at different flow rate scenarios.

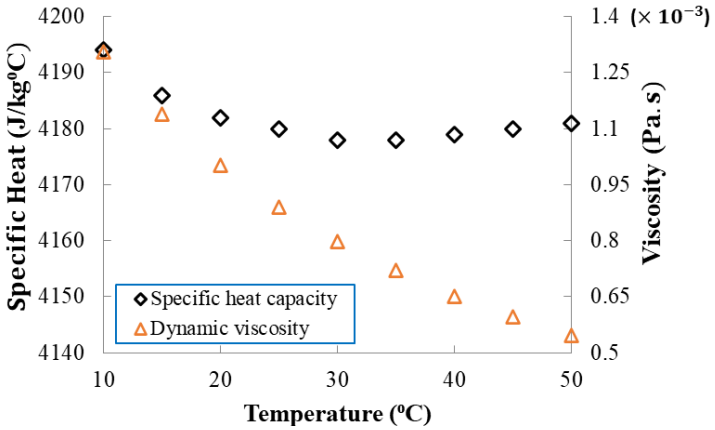

Figure 5. Variations in the thermophysical properties with respect to temperature level.

Reynolds numbers at the cold stream U-tube inlets vary between 105.7 and 1725.8 for a flow rate range of 50–500 L/h under 10–30 ℃ temperature levels. Therefore, the cold stream is assumed to be in a laminar flow regime for all investigated scenarios ($Re < Re_{cr}$). On the other hand, the hot stream Re number range is between 978.7 and 17,746.7 when the inlet temperature level changes from 20 ℃ to 50 ℃. The range indicates both laminar and turbulent flow regimes, yet it is obvious that the baffles in the shell domain cause vortices and mixture effects even in the low Re numbers. At this point, both the inviscid model and turbulence physics were applied for Re < 2300, and it was detected that the investigated turbulence models successfully cover the laminar flow regime conditions when $Re < Re_{cr}$. Thus, the turbulent flow regime conditions were set in the hot stream for each investigated scenario. Reynolds number calculations with variable thermophysical properties were conducted via the following equation [33,34]:

$$Re = \frac{\rho \underline{V} D_h}{\mu} = \frac{\underline{V} D_h}{\vartheta} \tag{10}$$

Table 3 presents the validation study results obtained via the experiments and numerical investigations. The results indicate that the discrepancy in hot stream outlet temperature varies between 0.47% and 2.92%, and the standard *k*-*ε* turbulence model provides proximate temperature levels in almost all scenarios. Furthermore, the pressure drop experienced by the U-tubes during the experiments is compared with the numerical data to improve the impact of the validation study. At a 50 L/h flow rate, the mean pressure drop during the experiments was measured at about 55.2 Pa, and it reached up to 682.8 Pa when the flow rate was 200 L/h. The numerical pressure drop levels are consistent with the experimental ones, and the values are 54.2 Pa and 694.4 Pa for the 50 L/h and 200 L/h flow rates, respectively. Note that the discrepancy

between the experimental and numerical pressure drop results varies between 3.65% and 9.18% (**Table 4**).

Table 4. Experimental and numerical pressure losses experienced at the cold and hot streams.

	$\Delta P_{c,\,exp}$ (Pa)	$\Delta P_{c,\,num}$ (Pa)	$\Delta P_{h,\,exp}$ (Pa)	$\Delta P_{h,\,num}$ (Pa)	Maximum discrepancy
50 L/h	55.2	54.2	6.7	6.2	7.46%
100 L/h	187.4	185.5	18.8	20.7	9.18%
200 L/h	682.8	694.4	73.9	71.2	3.65%
300 L/h	1574.5	1510.6	149.9	156.2	4.20%
400 L/h	2697.7	2681.2	275.8	265.6	3.69%
500 L/h	4303.3	4128.3	435.1	419.2	4.06%

2.4. ANN-aided multi-objective optimization via stochastic methods

In this work, nonlinear stochastic optimization algorithms of Differential Evolution (DE), Nelder-Mead (NM), Random Search (RS), and Simulated Annealing (SA) are utilized for the aim of a stochastic optimization process [37–39]. The best operating point providing enhanced overall performance is investigated via artificial neural network (ANN)-based data training and stochastic optimization methods. A nonlinear regression code has been developed in Wolfram Mathematica [40], and it is coupled with the stochastic optimization algorithms to determine the optimal operating point of the investigated shell-and-tube heat exchanger system. **Figure 6** shows the main steps and procedures for the optimization investigations.

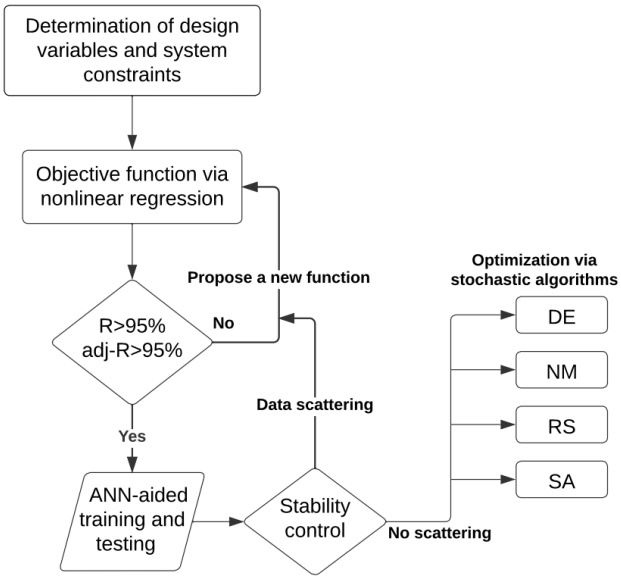

Figure 6. Flowchart of the ANN-aided optimization process.

In an optimization study, we need design variables, system constraints, and objective function(s) to capture the best possible solution. Cold/hot stream temperature levels and flow rates are the independent variables of this investigation, while the total volume of fluid, main dimensions and geometrical forms, and the total number of U-tubes within the shell and tube heat exchanger system are the design constraints. On the other hand, the proposed objective function represents the overall performance of

the system, which is the ratio of the thermal and hydraulic performances. At this point, various nonlinear regression models (such as logarithmic, polynomial, trigonometric, and rational forms) were tried in 1st, 2nd, and 3rd orders to check the best fit and statistical stability of the proposed objective function. Note that the 2nd-order rational model is detected as being in better agreement with the collected thermal and hydraulic performance data.

In the proposed nonlinear regression model, the *R*-square (R^2) and adjusted- R^2 values are over 96.3%, yet this is not sufficient to check the accuracy of the model. Once the objective function was determined, the ANN approach was utilized for the aim of checking the accuracy of the predictions. In this approach, 20% of data is considered as testing data, and this portion is randomly extracted from the whole data set [38]. On the other hand, the remaining data (80% of the total data set) is used for training purposes to minimize the discrepancies between the exact data points and the model outputs. In the ANN-aided optimization approach, the objective function is obtained via training data, and testing data is used for controlling the performance of the model in avoiding scattering points. This process is crucial for the optimization studies, as many researchers claim to have determined a local optimum without being aware of the scattering points. Once the model satisfies both the statistical (R^2 and adjusted-R^2) criteria and stability (ANN approach) control parameters, stochastic optimization algorithms of DE, NM, RS, and SA are coupled via a written code to get an optimal operating point providing the best overall performance.

3. Results and discussion

3.1. Thermal results

The shell and tube heat exchanger system has been investigated under various cold/hot stream temperature scenarios and flow rate conditions to observe the trend of thermal and hydraulic performance from experimental and numerical points of view. The Reynolds number experienced at the inlet of the U-tubes changes between 105.7 and 1725.6; therefore, the flow regime of the cold stream is laminar at each thermal and hydraulic scenario (50–500 L/h). On the other hand, hot stream calculations indicate that the 50 L/h flow rate case is the sole scenario of the laminar regime with a Re number range of 978.7 to 1774.8. Except for the 50 L/h flow rate, the hot stream Re number at the shell inlet varies between 1957.4 and 17,746.7. That is the reason for using a validated turbulence model at the hot water stream.

Figure 7 presents the heat transfer maps of the investigated thermal and hydraulic scenarios. The heat transfer rates of the cold and hot streams are calculated via:

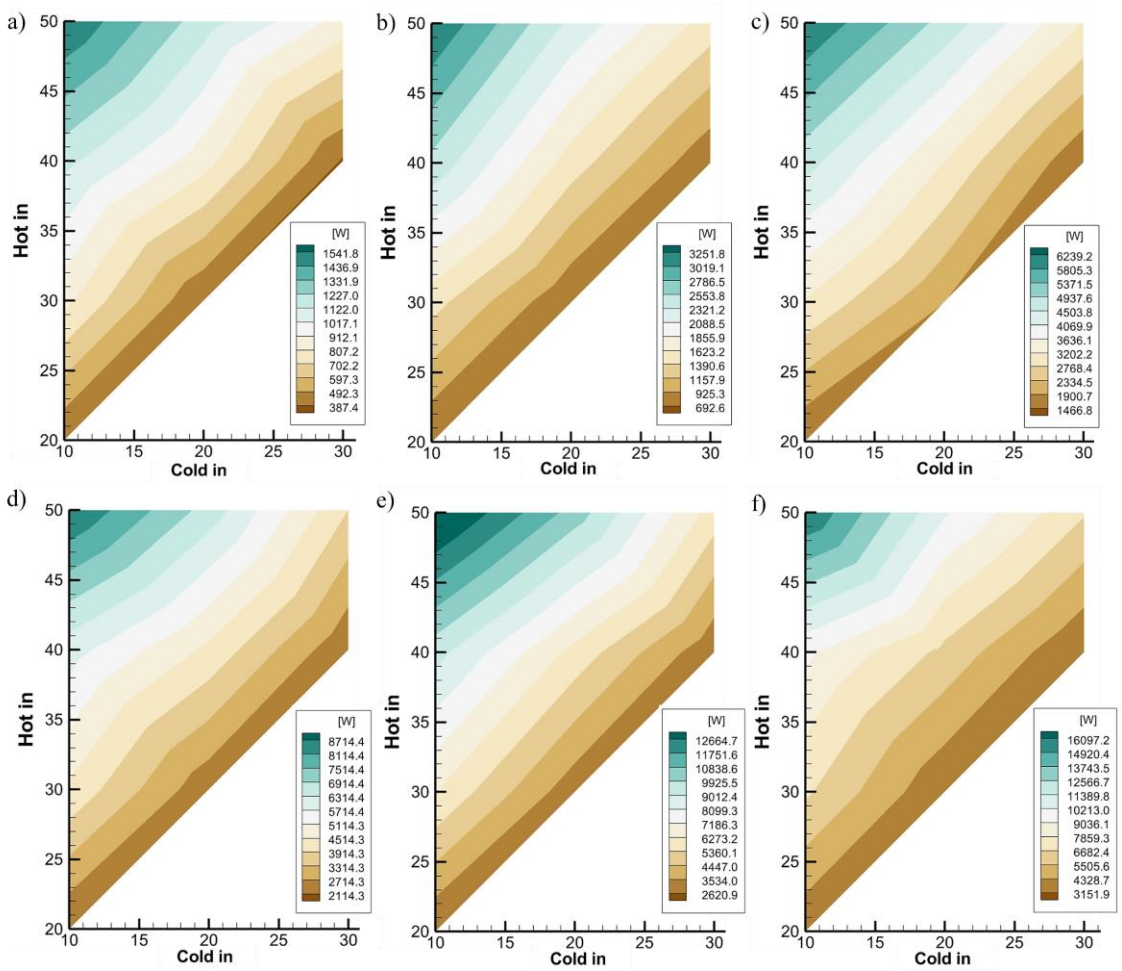

Figure 7. Amount of transferred heat when the flow rate is at **(a)** 50 L/h; **(b)** 100 L/h; **(c)** 200 L/h; **(d)** 300 L/h; **(e)** 400 L/h; **(f)** 500 L/h.

$$\dot{Q}_c = \dot{m}_c C_{p,c}\left(T_{c,out} - T_{c,in}\right) \tag{11}$$

$$\dot{Q}_h = \dot{m}_h C_{p,h}\left(T_{h,in} - T_{h,out}\right) \tag{12}$$

where $\dot{Q}$ denotes the heat transfer rate, $\dot{m}$ is the mass flowrate, and C_p is the specific heat at constant pressure. Note that the subscripts of c and h refer to cold and hot streams. The conservation of energy principle is applied to the shell and tube system to double-check the amount of heat transfer. In the experiments, the laboratory temperature level remained constant at 20 ℃ via a thermal control unit. In the numerical calculation, natural convection conditions are applied to the proposed validated shell and tube heat exchanger model to mimic the experimental conditions at the outer surfaces of the system. The convective heat transfer coefficient is determined from $Nu = 0.59Ra_H^{1/4}$ in natural convection when the Rayleigh number based on the wall height remains below 10^9 [34,41]. The heat transfer coefficient range based on natural convection physics is calculated to be between 10.42 W/m^{2}K and 13.71 W/m^{2}K for the investigated thermal scenarios. Convective heat transfer from the heat exchanger shell to the environment is calculated as follows:

$$\dot{Q}_{conv} = h\, A_s \left(T_{s,ave} - T_{\infty}\right) \tag{13}$$

where h is the convection heat transfer coefficient, A_s is the surface area, and $T_{s,ave}$ and T_{∞} are the mean surface temperature and free stream temperature, respectively.

Figure 8 shows the temperature maps of the shell and U-tubes at 10 ℃ cold stream-20 ℃ hot stream (C10H20) scenario. The results of the 50–200 L/h flow rate range indicate that the cold stream outlet temperature is always higher than the hot stream one, as the hot inlet directly affects the cold stream outlet section. Temperature level at the cold water outlet varies between 16.74 ℃ and 16.07 ℃ under 50 L/h, 100 L/h, and 200 L/h flow rates. The heat transfer rates measured at these volumetric flow rates are 387.4 W, 692.6 W, and 1466.8 W, respectively. Note that thermal dissipation on the steel shell is lower compared to the U-tube system as the tubes are made of copper.

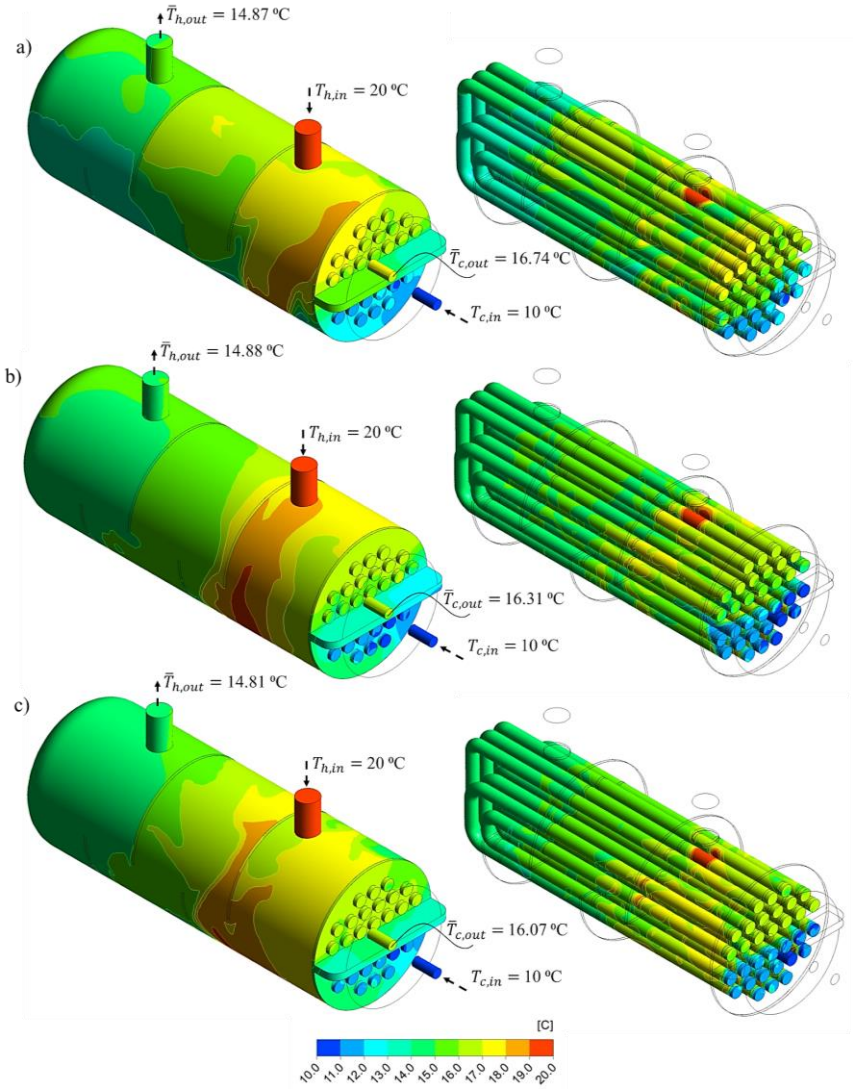

Figure 8. Temperature maps of the shell and U-tubes at 10 ℃ cold stream-20 ℃ hot stream (C10H20) scenario for **(a)** 50 L/h; **(b)** 100 L/h; **(c)** 200 L/h flow rates.

Likewise, the temperature maps of the identical thermal scenario (C10H20) are presented in **Figure 9** for high flow rates changing in a range of 300–500 L/h. Thermal

maps of the 300 L/h and 400 L/h scenarios are more uniform compared to the maximum case of 500 L/h. Note that the heat transfer rates experienced at these flow rates are 2114.3 W, 2620.9 W, and 3361.1 W, respectively. The thermal results given in **Figures 8** and **9** uncover that the outlet temperatures of the cold and hot streams slightly change with the flow rates, yet the heat transfer rates are dominantly affected by the rate of streams.

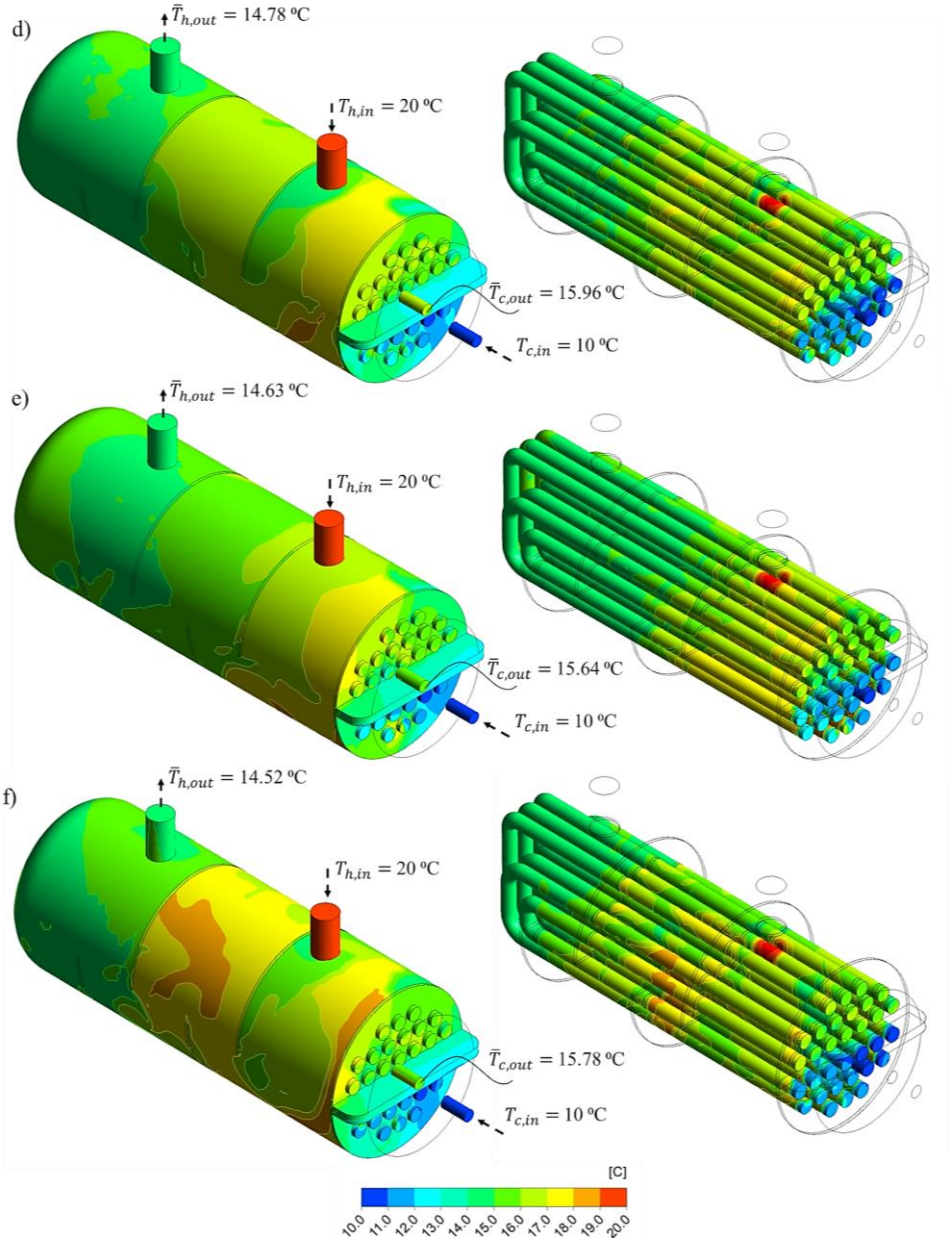

Figure 9. Temperature maps of the C10H20 scenario under **(d)** 300 L/h; **(e)** 400 L/h; **(f)** 500 L/h cold/hot stream flow rates.

The C10H20 scenario corresponds to the lowest temperature levels and minimum temperature difference case within the investigated thermal scenarios. All the thermal possibilities within a range of 10–30 ℃ cold stream temperature and 20–50 ℃ hot stream temperature are examined in detail for each 10 ℃ temperature difference. At this point, we reached the maximum temperature difference at 10 ℃ cold and 50 ℃

hot water temperature levels (C10H50). Note that the proposed numerical model was validated by the experimental data of C10H20, C10H30, C10H40, and C10H50 scenarios at various flow rates to improve the accuracy. The experimental results obtained via the temperature and pressure measurements on the cold and hot streams are documented in the Appendix for each investigated thermal and hydraulic scenario.

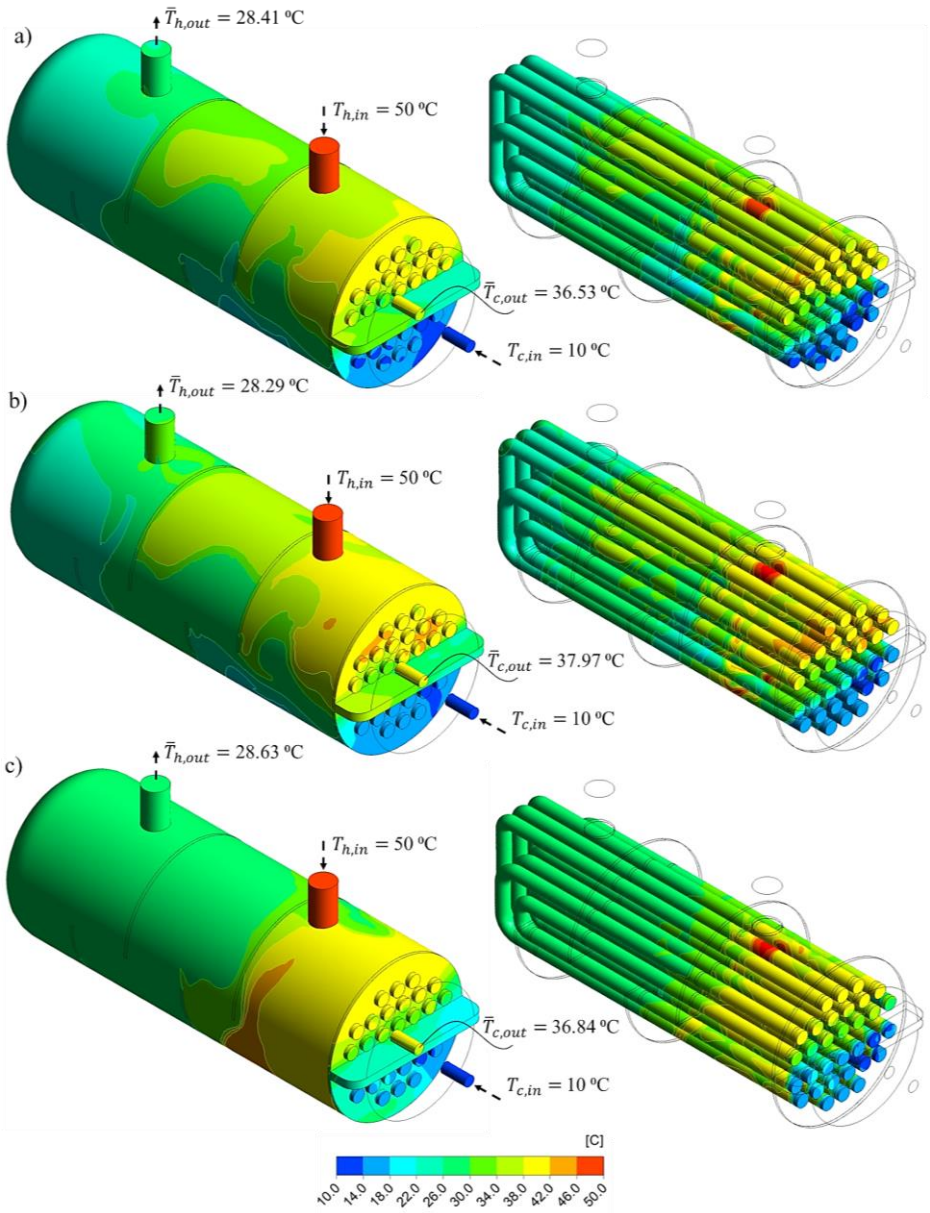

Figure 10. Temperature maps of the shell and U-tubes at 10 ℃ cold stream-50 ℃ hot stream (C10H50) scenario for **(a)** 50 L/h; **(b)** 100 L/h; **(c)** 200 L/h flow rates.

Figure 10 presents the temperature maps of the shell domain and U-tubes for the 10 ℃ cold stream-50 ℃ hot stream (C10H50) scenario. The thermal results of 50–200 L/h volume flow rates show that the trends observed at the cold and hot stream outlets are identical with C10H20 cases, i.e., the average outlet temperature level just after the U-tubes is always greater than the hot stream outlet temperature. The physical reason behind this phenomenon can be explained as hot fluid at the shell entrance sweeps the U-tube outlet section and transfers heat directly in an efficient way.

Therefore, even if the cold stream temperature is in a linear thermal tendency in most of the U-tube part, the temperature levels rise rapidly when the cold stream is getting closer to the U-tube outlet region. Furthermore, the segmental baffles within the shell structure contribute to conveying more heat from the hot fluid by circulating the hot stream. The findings indicate that the outlet temperature of the cold stream varies in a range of 36.53 ℃ and 37.97 ℃ under 50 L/h, 100 L/h, and 200 L/h flow rates. Moreover, heat transfer rates of the C10H50 scenarios at these flow rates are in a range of 1541.8 W to 6239.2 W. Note that the hot stream outlet temperature level slightly changes with the flow rates, which is a similar phenomenon observed at the C10H20 investigations.

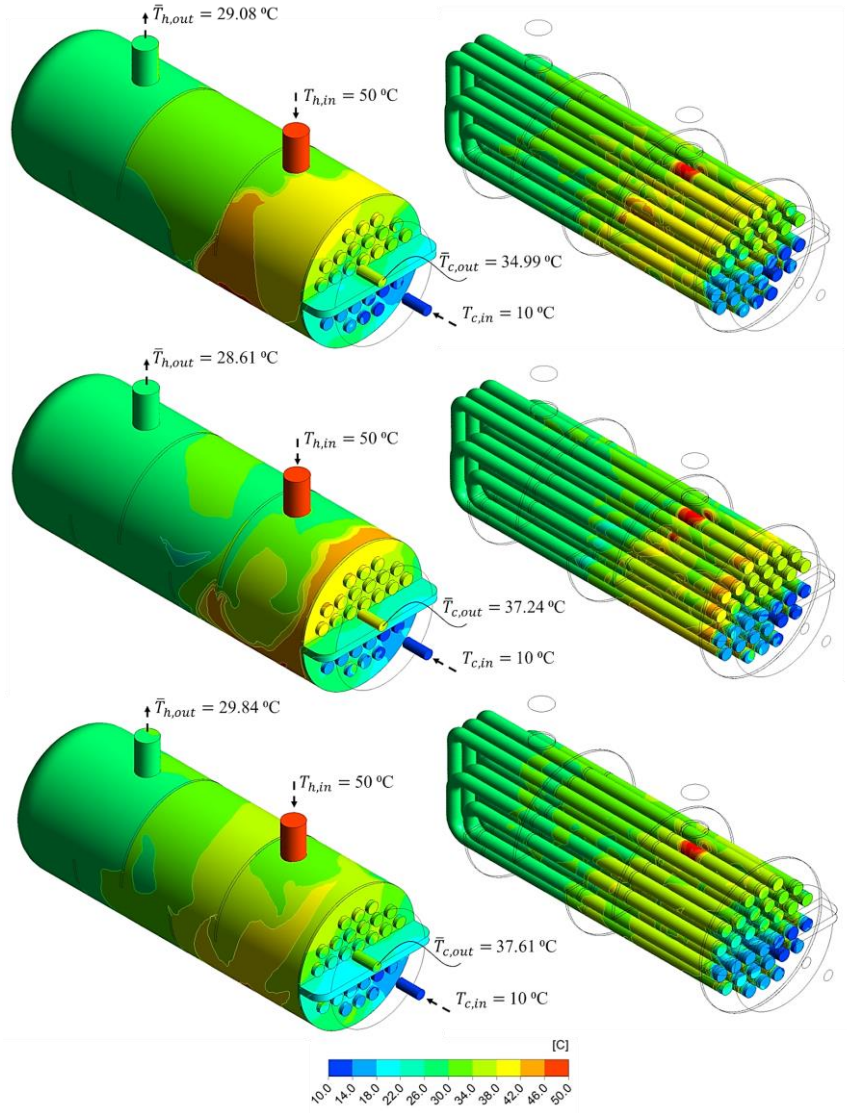

Figure 11. 10 ℃ cold stream-50 ℃ hot stream (C10H50) scenario under 300 L/h, 400 L/h, and 500 L/h cold/hot stream flow rates.

Figure 11 shows the C10H50 temperature maps under 300 L/h, 400 L/h, and 500 L/h cold/hot stream flow rates. The average temperature at the cold stream outlet is reported as 34.99 ℃ for the 300 L/h volumetric flow rate. The temperature level increases to 37.24 ℃ and 37.61 ℃ when the flow rates are 400 L/h and 500 L/h. In

parallel with the flow rate increase, the thermal distribution gets more homogenous in the 500 L/h scenario. The heat transfer rates measured at these flow rates rise to 8714.4 W, 12,664.7 W, and 16,097.2 W, respectively. However, enhancement of the thermal performance comes with additional pressure drop and pumping power; therefore, the total energy consumption should be considered in the evaluation of the overall performance. Note that all temperature maps covering the thermal and hydraulic scenarios are logged and presented in the Appendix. The overall results were evaluated in the stochastic optimization section.

3.2. Pressure drop and total energy consumption

In parallel with the thermal investigations, the pressure drop experienced at the shell and tube heat exchanger system was observed for various thermal and hydraulic scenarios. Pressure differences between the inlet and outlet of the cold and hot streams are monitored during the experiments by the precise manometers. Furthermore, total pressure drop obtained via the numerical models has been observed at distinct temperature and flow rate levels to improve the impact of the investigations. Note that the total pressure drop at identical flow rates slightly changes with the temperature levels due to the variations in thermophysical properties such as density and viscosity. On the other hand, variations in the cold and hot stream flow rates dominate the pressure losses experienced within the shell and tube heat exchanger systems.

Table 4 presents the experimental and numerical pressure drop of the cold and hot streams for the flow rate range of 50–500 L/h. The results show that numerical pressure drop levels are in conformity with the experimental ones. The discrepancy among the experimental measurements and numerical data varies between 3.65% and 9.18%. The hydraulic trend indicates the majority of the experimental measurements at greater pressure drop. The physical reason for this phenomenon can be explained with fouling possibilities on the cold and hot streamlines. Next, the pumping power required to push the cold and hot water streams is calculated as follows [34,41]:

$$\dot{W} = \Delta P \times \dot{V} \tag{14}$$

where $\dot{W}$ and $\dot{V}$ are the abbreviations of pumping power and volume flow rates, respectively. **Figure 12** presents the energy consumption levels of the cold and hot fluid streams for the flow rates altering between 50 L/h and 500 L/h. The results given in **Figure 12a**,**b** show that the energy consumption experienced at the U-tubes is always greater (about 10 times) than the hot stream ones at identical flow rates. The maximum level of energy consumption reaches up to 2064.2 Wh when the flow rate of the cold water stream is 500 L/h.

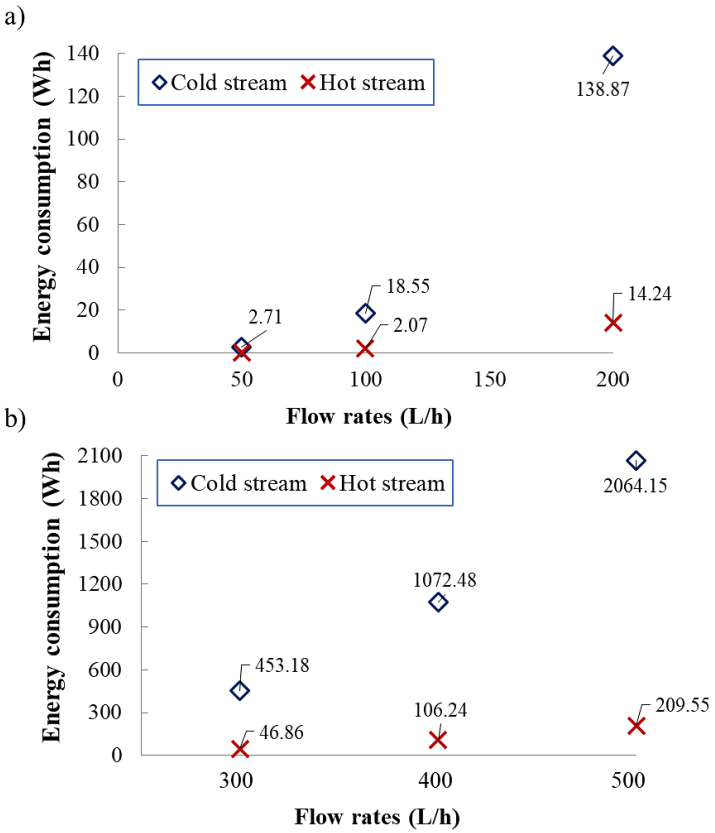

Figure 12. Energy consumption of the cold and hot streams in the flow rate range of **(a)** 50–200 L/h; **(b)** 300–500 L/h.

3.3. ANN-aided stochastic optimization results

In the current work, experimental and numerical results are utilized to obtain an optimal operating point satisfying an enhanced overall performance. Stochastic optimization refers to the process of finding the optimal value of a function when one or more of its input parameters are governed by probabilistic or random behavior. The stochastic optimization algorithms of Differential Evolution (DE), Nelder-Mead (NM), Random Search (RS), and Simulated Annealing (SA) are coupled with the ANN approach to avoid local scattering and provide model robustness. All four algorithms do not require gradient or derivative information, making them well-suited for optimizing non-differentiable functions. Furthermore, they use iterative approaches inspired by natural or intuitive processes. Overall performance (η) corresponds to the ratio of dimensionless thermal performance and dimensionless pumping power, which can be calculated as follows:

$$\eta = \frac{\frac{\dot{Q}}{\dot{Q}_{max}}}{\frac{1}{2}\left(\frac{\dot{W}_c}{\dot{W}_{c,max}} + \frac{\dot{W}_h}{\dot{W}_{h,max}}\right)} \tag{15}$$

Wolfram Mathematica [40] is utilized to develop a code by combining regression, an ANN approach, and stochastic optimization algorithms. As discussed in section 2.3, various nonlinear regression models (such as logarithmic, polynomial, trigonometric,

and rational forms) were tried in 1st, 2nd, and 3rd orders to check the best fit and statistical stability of the proposed objective function. Note that the 2nd-order rational model satisfied the statistical evaluations (≥ 96.3%), stability checks, and ANN-aided scattering controls. The proposed objective function (Φ) is given as follows:

$$\Phi = \frac{a_0 + a_1x_1 + a_2x_2 + a_3x_3 + a_4x_1x_2 + \ldots + a_{13}x_3^2 + a_{14}x_4^2}{b_0 + b_1x_1 + b_2x_2 + b_3x_3 + b_4x_1x_2 + \ldots + b_{13}x_3^2 + b_{14}x_4^2} \quad (16)$$

Here, x_1 and x_2 represent the cold and hot stream inlet temperature levels (ºC), respectively. The cold and hot volume flow rates are denoted by x_3 and x_4, and coefficients of the objective function are symbolized via a and b. **Table 5** presents the coefficients of the 2nd-order rational model.

Table 5. Coefficients of the optimization study objective function.

	0	**1**	**2**	**3**	**4**	**…**	**13**	**14**
a	3712.85	1663.54	−1786.33	−4.2912	−4.2921	…	−0.0108	−0.0109
b	−319.17	−45.599	−66.513	−61.967	−61.962	…	0.1636	0.1569

The experimental and numerical results uncover that the maximum heat transfer occurs at a 500 L/h flow rate when the cold stream inlet temperature is at 10 °C and hot fluid enters at 50 °C, yet it also comes with additional pressure losses corresponding to an elevated energy consumption. At this point, the overall performance concept considers both thermal performance and energy consumption under laminar and turbulent flow regime conditions; therefore, the physical phenomenon is nonlinear. In the optimization process, the Nelder-Mead algorithm provided the optimal operating point at about 105 s, while the total duration reached up to 143 s via the Random Search algorithm. The overall performance results varied between 0.195 and 6.878, and all stochastic optimization algorithms detected the same point as optimal. The best operating point with a 6.878 overall performance value is achieved at the C10H50 thermal scenario when the cold and hot stream flow rates are 100 L/h and 500 L/h, respectively. As the U-tubes dominantly affect the total energy consumption experienced within the shell and tube heat exchanger system, maximization of the cold stream flow rate doesn't contribute to the overall performance after 100 L/h. Note that the worst case with 0.195 overall performance was obtained in the C30H40 scenario with 500 L/h identical flow rate at the cold and hot streams. The present methodology and main findings are in line with shell and tube heat exchanger literature. After evaluating many turbulence models from thermal and hydraulic perspectives, the *k-ε* turbulence model was selected due to excellent matches, as emphasized by Ozden and Tari [24]. Furthermore, the objective function strategy and statistical controls are similar to shell and tube heat exchanger optimization studies in the literature [28,29].

4. Conclusion

This study provides a novel methodology to integrate the experimental measurements, numerical findings, and ANN-aided stochastic optimization algorithms for an industrial shell and tube heat exchanger system. Thermal and

hydraulic performance of the investigated system have been examined under various temperature and flow rate conditions. Furthermore, the optimal operating point was obtained via coupling the nonlinear regression models, statistical checks, ANN-aided stability control, and stochastic optimization algorithms. The highlights of the current study are given as follows:

- Experimental measurements and numerical findings are in good agreement from the heat transfer rate and pressure drop points of view. The discrepancy among the experimental measurements and numerical data varies between 0.033% and 9.18%.
- Cold stream (U-tubes) flow rate dominantly affects the overall energy consumption within the investigated shell and tube system. The pressure drop experienced at the hot stream is about 1/10 of the cold one at an identical level.
- Variations in the cold and hot stream inlet temperature levels have a negligible impact on the overall energy consumption. Mean pressure drop values are documented in **Table 4** for a flow rate range of 50–500 L/h.
- Although the case satisfying improved heat transfer rate is predictable, the energy consumption shall also be considered as it directly affects the operational cost. The overall performance couples the heat transfer rate and pumping power, and it varies between 0.195 and 6.878 for the investigated shell and tube system.
- The C10H50 scenario with 100 L/h cold stream and 500 L/h hot stream flow conditions was detected as the optimal operating point via the stochastic optimization algorithms ($\eta \approx 6.878$).

Conflict of interest: The author declares no conflict of interest.

Nomenclature

A		heat transfer surface area [m^2]
	C_p	specific heat capacity [J kg^{-1} K^{-1}]
C		turbulent flow coefficients
	D_h	hydraulic diameter [m]
g		gravitational acceleration [m s^{-2}]
k		turbulent kinetic energy [m^2 s^{-2}]
	$\dot{m}$	mass flow rate [kg/s]
P		pressure [Pa]
	$\dot{Q}$	heat generation [W]
Re		Reynolds number
S		source term
T		temperature [K]
	T'	turbulent temperature fluctuation [m s^{-1}]
	$\underline{V}$	average velocity [m s^{-1}]

$\underline{u}$	mean velocity in x-direction [m s^{-1}]
u'	turbulent fluctuation in x-direction [m s^{-1}]
V	velocity vector
v	velocity in y-direction [m s^{-1}]
$\underline{v}$	mean velocity in y-direction [m s^{-1}]
v'	turbulent fluctuation in y-direction [m s^{-1}]
$\dot{V}$	volumetric flow rate [m^{3}s^{-1}]
$\dot{W}$	pumping power [W]
w	velocity in z-direction [m s^{-1}]
$\underline{w}$	mean velocity in z-direction [m s^{-1}]
w'	turbulent fluctuation in z-direction [m s^{-1}]

Greek letters

α	thermal diffusivity [m^2 s^{-1}]
ε	eddy dissipation rate [m^2 s^{-3}]
ρ	density [kg m^{-3}]
ϕ	diameter [m]
Φ	objective function
μ	dynamic viscosity [Pa s]
μ_t	eddy viscosity [m^2 s^{-1}]
ϑ	kinematic viscosity [m^2 s^{-1}]
σ_k	turbulent Prandtl number for k
σ_ε	turbulent Prandtl number for ε
σ_{cp}	turbulent Prandtl number based on specific heat at constant pressure

Abbreviations

ANN	Artificial Neural Network
COP	Climate Change Conference
DE	Differential Evolution algorithm
HVAC-R	heating, ventilation, air conditioning and refrigeration
NM	Nelder-Mead algorithm
RS	Random Search algorithm
SA	Simulated Annealing

Subscripts

ave	average value
c	cold stream
conv	convection
f	fluid medium
h	hot steam
i	*i*th component of the vector field
in	inlet
j	*j*th component of the vector field
out	outlet
s	heat transfer surface

References

1. United Nations. In: Proceedings of the United Nations Climate Change Conference (COP27); 2023.
2. International Energy Agency. Renewable Electricity Technical Report. Available online: https://www.iea.org/reports/renewable-electricity (accessed on 15 March 2025).
3. International Energy Agency. Buildings Technical Report. Available online: https://www.iea.org/reports/buildings (accessed on 15 March 2025).
4. Chenari B, Dias Carrilho J, Gameiro da Silva M. Towards sustainable, energy-efficient and healthy ventilation strategies in buildings: A review. Renewable and Sustainable Energy Reviews. 2016; 59: 1426–1447. doi: 10.1016/j.rser.2016.01.074
5. Tian J, Yu L, Xue R, et al. Global low-carbon energy transition in the post-COVID-19 era. Applied Energy. 2022; 307: 118205. doi: 10.1016/j.apenergy.2021.118205
6. Taş E, Güngör Ş. Design and analytical investigation on air-to-air cross flow heat exchanger of an industrial heat recovery ventilation system. Scientia cum Industria. 2023; 11(1): e231103. doi: 10.18226/23185279.e231103
7. Said Z, Rahman S, Sharma P, et al. Performance characterization of a solar-powered shell and tube heat exchanger utilizing MWCNTs/water-based nanofluids: An experimental, numerical, and artificial intelligence approach. Applied Thermal Engineering. 2022; 212: 118633. doi: 10.1016/j.applthermaleng.2022.118633
8. Laszczyk P. Simplified modeling of liquid-liquid heat exchangers for use in control systems. Applied Thermal Engineering. 2017; 119: 140–155. doi: 10.1016/j.applthermaleng.2017.03.033
9. Yang X, Guo J, Zhao S, et al. High shear mixer works as a heat exchanger enhancing the liquid–liquid direct contact heat transfer. International Journal of Heat and Mass Transfer. 2023; 200: 123547. doi: 10.1016/j.ijheatmasstransfer.2022.123547
10. Fratczak M, Czeczot J, Nowak P, et al. Practical validation of the effective control of liquid–liquid heat exchangers by distributed parameter balance-based adaptive controller. Applied Thermal Engineering. 2018; 129: 549–556. doi: 10.1016/j.applthermaleng.2017.10.056
11. Jige D, Sugihara K, Inoue N. Evaporation heat transfer and flow characteristics of vertical upward flow in a plate-fin heat exchanger. International Journal of Refrigeration. 2022; 133: 165–171. doi: 10.1016/j.ijrefrig.2021.09.030
12. Węglarz K, Taler D, Taler J. New non-iterative method for computation of tubular cross-flow heat exchangers. Energy. 2022; 260: 124955. doi: 10.1016/j.energy.2022.124955
13. Geoffroy H, Berger J, Gonze E, et al. Experimental dataset for an AHU air-to-air heat exchanger with normal and simulated fault operations. Journal of Building Performance Simulation. 2022; 16(3): 268–290. doi: 10.1080/19401493.2022.2097311
14. Lee S, Chung Y, Jeong Y, et al. Investigation on the performance enhancement of electric vehicle heat pump system with air-to-air regenerative heat exchanger in cold condition. Sustainable Energy Technologies and Assessments. 2022; 50: 101791. doi: 10.1016/j.seta.2021.101791
15. Zeng C, Liu S, Shukla A. A review on the air-to-air heat and mass exchanger technologies for building applications. Renewable and Sustainable Energy Reviews. 2017; 75: 753–774. doi: 10.1016/j.rser.2016.11.052
16. Tang F, Nowamooz H. Factors influencing the performance of shallow Borehole Heat Exchanger. Energy Conversion and Management. 2019; 181: 571–583. doi: 10.1016/j.enconman.2018.12.044

17. Kim M, Ha MY, Min JK. A numerical study on various pin–fin shaped surface air–oil heat exchangers for an aero gas-turbine engine. International Journal of Heat and Mass Transfer. 2016; 93: 637–652. doi: 10.1016/j.ijheatmasstransfer.2015.10.035
18. Alrwashdeh SS, Ammari H, Madanat MA, et al. The Effect of Heat Exchanger Design on Heat transfer Rate and Temperature Distribution. Emerging Science Journal. 2022; 6(1): 128–137. doi: 10.28991/esj-2022-06-01-010
19. Ariyo DO, Bello-Ochende T. Constructal design of two-phase stacked microchannel heat exchangers for cooling at high heat flux. International Communications in Heat and Mass Transfer. 2021; 125: 105294. doi: 10.1016/j.icheatmasstransfer.2021.105294
20. Jin Y, Gao N, Zhu T. Controlled variable analysis of counter flow heat exchangers based on thermodynamic derivation. Applied Thermal Engineering. 2018; 129: 684–692. doi: 10.1016/j.applthermaleng.2017.10.025
21. Mangrulkar CK, Dhoble AS, Chamoli S, et al. Recent advancement in heat transfer and fluid flow characteristics in cross flow heat exchangers. Renewable and Sustainable Energy Reviews. 2019; 113: 109220. doi: 10.1016/j.rser.2019.06.027
22. Feng CN, Liang CH, Li ZX. Friction factor and heat transfer evaluation of cross-corrugated triangular flow channels with trapezoidal baffles. Energy and Buildings. 2022; 257: 111816. doi: 10.1016/j.enbuild.2021.111816
23. Wang S, Wen J, Li Y. An experimental investigation of heat transfer enhancement for a shell-and-tube heat exchanger. Applied Thermal Engineering. 2009; 29(11-12): 2433–2438. doi: 10.1016/j.applthermaleng.2008.12.008
24. Ozden E, Tari I. Shell side CFD analysis of a small shell-and-tube heat exchanger. Energy Conversion and Management. 2010; 51(5): 1004–1014. doi: 10.1016/j.enconman.2009.12.003
25. Wang Q, Chen Q, Chen G, et al. Numerical investigation on combined multiple shell-pass shell-and-tube heat exchanger with continuous helical baffles. International Journal of Heat and Mass Transfer. 2009; 52(5-6): 1214–1222. doi: 10.1016/j.ijheatmasstransfer.2008.09.009
26. Abbasian Arani AA, Moradi R. Shell and tube heat exchanger optimization using new baffle and tube configuration. Applied Thermal Engineering. 2019; 157: 113736. doi: 10.1016/j.applthermaleng.2019.113736
27. Gao B, Bi Q, Nie Z, et al. Experimental study of effects of baffle helix angle on shell-side performance of shell-and-tube heat exchangers with discontinuous helical baffles. Experimental Thermal and Fluid Science. 2015; 68: 48–57. doi: 10.1016/j.expthermflusci.2015.04.011
28. Costa ALH, Queiroz EM. Design optimization of shell-and-tube heat exchangers. Applied Thermal Engineering. 2008; 28(14-15): 1798–1805. doi: 10.1016/j.applthermaleng.2007.11.009
29. Patel VK, Rao RV. Design optimization of shell-and-tube heat exchanger using particle swarm optimization technique. Applied Thermal Engineering. 2010; 30(11-12): 1417–1425. doi: 10.1016/j.applthermaleng.2010.03.001
30. Ponce-Ortega JM, Serna-González M, Jiménez-Gutiérrez A. Use of genetic algorithms for the optimal design of shell-and-tube heat exchangers. Applied Thermal Engineering. 2009; 29(2-3): 203–209. doi: 10.1016/j.applthermaleng.2007.06.040
31. Gungor S. Experimental comparison on energy consumption and heat transfer performance of corrugated H-type and L-type brazed plate heat exchangers. International Communications in Heat and Mass Transfer. 2023; 144: 106763. doi: 10.1016/j.icheatmasstransfer.2023.106763
32. Turhan C, Çeter AE. A novel occupant detection-based ventilation control strategy for smart building applications. Mugla Journal of Science and Technology. 2021; 7(2): 24–35. doi: 10.22531/muglajsci.928315
33. Fox RW, McDonald AT, Pritchard PJ, Mitchell JW. Introduction to Fluid Mechanics. Wiley; 2014.
34. Bejan A. Convection Heat Transfer. Wiley; 2013.
35. Stanford University. Turbulent flow technical report. Available online: https://web.stanford.edu/class/me469b/handouts/turbulence.pdf (accessed on 15 March 2025).
36. ANSYS, Inc. ANSYS Fluent Theory Guide, Release 18.2. ANSYS, Inc; 2017.
37. Güngör S, Ceyhan U, Karadeniz ZH. Optimization of heat transfer in a grooved pipe model by Stochastic Algorithms and DOE based RSM. International Journal of Thermal Sciences. 2021; 159: 106634. doi: 10.1016/j.ijthermalsci.2020.106634
38. Aydin L, Artem HS, Oterkus S. Designing engineering structures using stochastic optimization methods. CRC Press; 2020.
39. Cavazzuti M. Optimization Methods: From theory to design scientific and technological aspects in mechanics. Springer Berlin Heidelberg; 2013.
40. Wolfram Research, Inc. Wolfram Mathematica, Release 11.3. Wolfram Research, Inc; 2018.
41. Incropera FP, Dewitt DP, Bergman TL, Lavine AS. Principles of Heat and Mass Transfer. Wiley; 2017.

Appendix

Table A1. Experimental results of the investigated thermal and hydraulic scenarios.

	Cold inlet (°C)	**Cold outlet (°C)**	**Hot inlet (°C)**	**Hot outlet (°C)**	**Cold stream ΔP (Pa)**	**Hot stream ΔP (Pa)**
	50 L/h flow rate at the cold and hot streams					
C10-H20	10.02	16.68	20.06	14.93	55	6
C10-H30	10.04	24.41	30.11	20.08	54	6
C10-H40	10.07	29.83	39.90	24.81	57	5
C10-H50	9.98	36.49	50.08	28.73	55	7
C20-H30	20.03	26.71	30.17	24.62	55	5
C20-H40	20.13	34.77	40.07	29.85	56	6
C20-H50	20.02	40.08	49.93	34.39	54	6
C30-H40	29.95	36.39	40.19	34.71	56	6
C30-H50	30.23	44.92	50.13	39.13	55	6
	100 L/h flow rate at the cold and hot streams					
C10-H20	10.03	15.91	20.14	14.81	185	18
C10-H30	9.96	22.93	30.17	19.36	187	18
C10-H40	9.98	31.35	39.97	24.08	185	19
C10-H50	10.03	37.62	50.02	28.69	191	20
C20-H30	20.14	25.97	30.09	24.92	184	18
C20-H40	20.09	32.90	39.94	29.28	188	18
C20-H50	19.86	39.31	50.03	34.45	186	20
C30-H40	30.16	36.13	40.18	34.83	190	20
C30-H50	30.08	42.84	50.05	39.36	191	18
	200 L/h flow rate at the cold and hot streams					
C10-H20	9.99	15.83	20.05	14.94	685	74
C10-H30	10.05	23.60	30.13	19.41	680	72
C10-H40	10.08	30.29	39.91	24.19	685	72
C10-H50	10.02	36.45	50.16	28.32	685	74
C20-H30	20.11	25.87	30.03	24.46	690	74
C20-H40	20.08	33.69	40.15	29.17	680	76
C20-H50	19.93	39.81	50.13	33.98	675	74
C30-H40	30.04	36.67	40.09	34.66	685	75
C30-H50	30.08	43.02	50.14	38.91	680	74

Table A1. (*Continued*).

	Cold inlet (℃)	Cold outlet (℃)	Hot inlet (℃)	Hot outlet (℃)	Cold stream ΔP (Pa)	Hot stream ΔP (Pa)
	300 L/h flow rate at the cold and hot streams					
C10-H20	10.07	15.87	20.13	14.66	1580	145
C10-H30	10.12	21.35	30.01	19.27	1560	148
C10-H40	10.09	26.49	40.09	24.31	1490	152
C10-H50	10.16	34.54	49.97	28.86	1590	146
C20-H30	19.97	26.17	30.02	24.65	1600	156
C20-H40	20.03	31.94	40.20	29.73	1550	150
C20-H50	20.10	38.83	50.11	33.88	1600	152
C30-H40	30.05	35.77	40.05	34.42	1580	152
C30-H50	29.98	40.68	49.93	39.46	1620	148
	400 L/h flow rate at the cold and hot streams					
C10-H20	9.91	15.37	20.16	14.68	2610	283
C10-H30	10.05	24.95	29.91	19.73	2580	280
C10-H40	10.13	29.86	40.04	24.33	2720	272
C10-H50	10.12	36.66	50.19	29.05	2740	285
C20-H30	20.17	26.01	30.08	24.41	2700	270
C20-H40	20.15	32.70	40.11	29.92	2750	270
C20-H50	20.09	41.98	50.03	33.88	2690	272
C30-H40	29.96	35.75	40.20	34.79	2750	278
C30-H50	30.08	41.94	50.25	39.43	2740	270
	500 L/h flow rate at the cold and hot streams					
C10-H20	10.05	15.65	20.14	13.96	4310	435
C10-H30	10.13	21.58	30.07	20.04	4340	428
C10-H40	9.88	25.31	40.02	24.73	4290	433
C10-H50	10.06	36.90	50.21	30.11	4360	441
C20-H30	20.01	25.44	29.85	25.02	4280	438
C20-H40	20.00	30.26	40.17	29.79	4310	435
C20-H50	20.12	37.29	50.07	35.03	4260	438
C30-H40	29.98	35.55	40.19	34.94	4290	430
C30-H50	30.09	41.60	50.22	40.08	4290	438